UNIVERSITY OF OKLAHOMA

GRADUATE COLLEGE

TOWARDS THE USAGE OF QUARRY BLASTS AS ACTIVE SEISMIC SOURCE

A THESIS

SUBMITTED TO THE GRADUATE FACULTY

in partial fulfillment of the requirements for the

Degree of

MASTER OF SCIENCE

By

PEIYAO LI
Norman, Oklahoma
2018

TOWARDS THE USAGE OF QUARRY BLASTS
AS ACTIVE SEISMIC SOURCE

A THESIS APPROVED FOR THE
CONOCOPHILLIPS SCHOOL OF GEOLOGY AND GEOPHYSICS

BY

Dr. Nori Nakata, Chair

Dr. Xiaowei Chen

Dr. Brett Carpenter

Acknowledgements

I would like to show how grateful I am to work with my advisor Dr. Nori Nakata, he is such a great researcher. What he has showed me is not only the world of Geophysics, but also how to be a good researcher in my future career. His advice on both of my research and life are priceless, and it's my great honor to work under his guidance, words cannot show my appreciation to Nori. He also provides me a lot of opportunities to explore the world of geophysics, hence, the content in this thesis could not cover all my work during my master candidate term.

I would also want to express my gratitude to my committee members Dr.Xiaowei Chen and Dr. Brett Carpenter for not only serving as my committee members, but also providing their expertise, insightful comments, and encouragement during my master career.

Additionally, I appreciate everyone in our research group: Raymond Ng, Jianhang Yin, Alexandro Vera, Stephen Marsh. All the discussions and suggestions in my master career benefits me a lot. I also want to thank Jiewen Zhang and Yan Qin for the help as well. I am very glad I meet these talented people, and work, study with them.

Last but more importantly, I want to thank my family: my parents and my fiancée,Keyi especially, for their spiritual support, it means a lot to me.

Table of Contents

List of Tables

List of Figures

Abstract

Active seismic sources are often used to obtain subsurface structure via seismic imaging. The geophone's capability to capture signals at lower frequencies is significantly improved, thus, we are no longer restricted to use the conventional seismic source for imaging. Hence, the choice of the seismic source can shift to an unconventional seismic source, such as the traffic noise, slow-slip events, and quarry blasts, and all these choices are economical and environmental friendlier. For the intention of obtaining the better understanding of subsurface structure in Mills Creek, southern Oklahoma, we designed a receiver line of 72 receivers with spacing of 105m, and the total length of 7,455m, located 120m away from the west side of the quarry exploitation field for 28 days. Here, we use the quarry blasts as an active seismic source and propose a workflow to extract the information that is essential for seismic imaging, such as the source wavelet, wave type identification, origin time and location estimation, we also discuss the observed structure in the study area.

Chapter 1: Introduction

Active seismic sources such as vibroseis, dynamite, and airgun, which are often placed at the surface or near-surface are categorized as man-made sources and used for obtaining the earth's structural response via seismic imaging (Berkhout and Verschuur 2011). Given the rapid technology development in the past decades, the geophone's capability of capturing the signal has significantly improved, and hence we can detect the signals at much lower frequencies than their natural frequency (G. Li et al. 2017).With more advanced geophones, we are no longer restricted by the sources, especially for academic researchers, since active seismic acquisition is usually expensive. There are numerous types of sources that are not primarily made for the purpose of seismic imaging, such as army weapon test and quarry blast, and also some unconventional seismic sources such as signals from railroads, the ocean, and slow-slip events (Nakata et al. 2011; Quiros, Brown, and Kim 2016; Reshetnikov, Buske, and Shapiro 2010; Xu et al. 2012). Although these signals are not intended for seismic imaging of the subsurface, we are able to use such signals into shot gathers that is applicable for conventional active source seismic imaging, by knowing certain information such as the origin time and distance, then applying appropriate algorithm, and image condition (i.e. wave mode extrapolation/separation). It's necessary to quantify the energy level of the source, the type of waves, the wave velocity, and more importantly, the origin time and distance of source to the geophone. Hence, by estimating this information, we can process the signal using conventional approaches, such as, stacking, wave mode separation, refraction survey, and the origin time and distance ensure the accuracy of the velocity and resolution of underground structure.

Differentiation of quarry blast signals from earthquake signals is a well-studied problem by earthquake seismologists, e.g. (Fereidoni and Atkinson 2017; B. Li et al. 2017; Shashidhar et al. 2014), and the methods to isolate the quarry blasts from catalog are mainly to incorporate the

seismic spectra (Yilmaz et al., 2013), where the corner frequency of the spectra from delayed quarry blast is lower than a microseismic event with same magnitude. Also for non-delay quarry blast which basically is one shot at the time, the spectra shows lower energy compared than an earthquake event (Smith 1993). However, the source used for mining and quarry exploration is an explosive and compressional source, the primary purpose of it is to spall rock face for easier exploitation, but the application of the seismic waves generated by the quarry blasts to seismic imaging has not been effectively used. Therefore, proper and utilization of the quarry blast energy as an active source is an economical and efficient way to understand the subsurface structure.

Here, I use the observed seismic waves generated by quarry blasts in Oklahoma to examine their wave types, propose a workflow to extract the information necessary for active-source imaging (e.g. origin time and location of the quarry blasts), and discuss the observed subsurface structure in the area. The workflow proposed here can be applied to any different quarry blasts.

Chapter 2: Data acquisition

2.1 Geology of study area

The study site is along high way 7, in the Mill Creek area of the Tishomingo Anticline, southern Oklahoma as shows in figure 1 (a), where hummocky outcrops of the crystalline basement dominate the topography. This basement is part of the 1350-1400 Ma Southern Granite-Rhyolite province of the US mid-continent, and is composed of granites, rhyolites and their metamorphic derivatives(Bickford et al. 2015). Since its emplacement in the Early Proterozoic, the basement has undergone multiple phases of tectonic deformation that include a rifting episode in the Late Proterozoic to Middle Cambrian resulting in the development of a NW-SE trending magmatic rift system in south-west Oklahoma, known as the Southern Oklahoma Aulacogen (Brewer et al. 1983). Late Paleozoic tectonic phases, which certainly affected the crystalline basement, involved compressional stresses that resulted in the inversion of the rift-bounding faults (Brewer et al. 1983). This Late Paleozoic tectonism produced major basement-involved uplifts in southern Oklahoma, among which is the Arbuckle Uplift. The Arbuckle Uplift is composed of several anticlinal domains including the Tishomingo Anticline, at the center of which the Precambrian basement is exposed in a region of ~300 km^2. The folded structures are bounded by faults that dominantly strike NW-SE (~300°) (Ham *et al*., 1964; Denison, 1995). The basement exposures include granites, granodiorites and gneisses that are locally cross-cut by sub-vertical and sub-horizontal pegmatite and diabase intrusions of Precambrian and Cambrian ages (Denison, 1995; Lidiak *et al*., 2014). The predominant NW-SE trend of sub-vertical dikes were influenced by the pre-existing structural fabric of the Precambrian basement (Denison, 1995; Lidiak *et al*., 2014). Field observations of the exposed granites reveal 10 cm - 10 m thicknesses for the sub-vertical and sub-horizontal intrusions shown in figure 1 (b), and 8 - 80 m -wide fault damage zones

characterized by dense parallel fracture clusters, epidote vein mineralization and pulverized zone at the core (Kolawole et al., 2018).

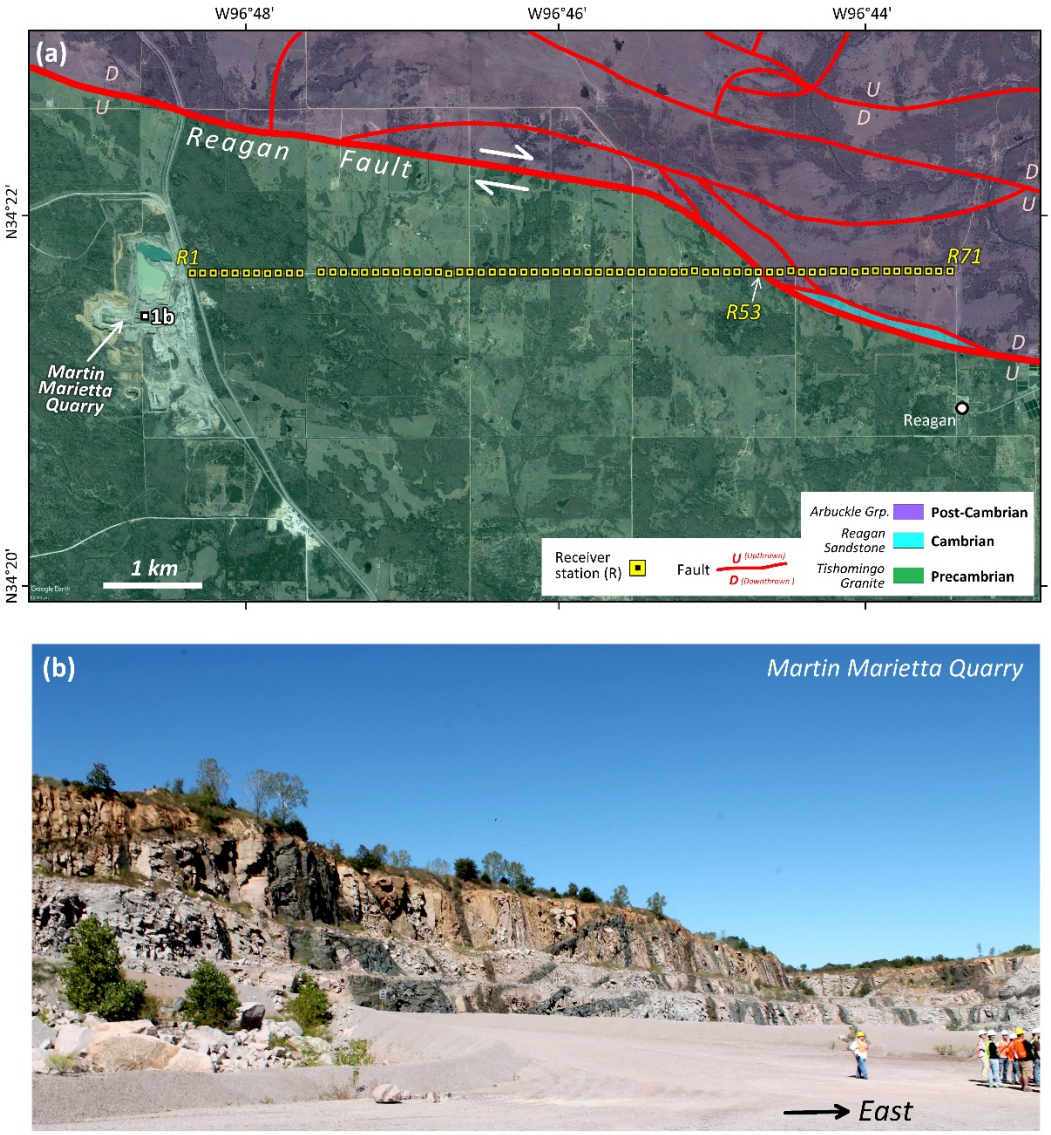

Figure 1: (a) Satellite image (Google Earth©) of the study area near, overlaid with generalized basement geology (after Ham & Mckiney, 1954) and the receiver array. (b) Photograph showing surface exposure of the basement at the

Martin Marietta Quarry. See “1b” in Fig.1a for location. Light-coloured rocks are granites; dark-coloured sub-vertical and dipping bands are diabase dikes and inclined sheets.

2.2 Seismic data acquisition

The objective of our study is to use quarry blasts as an active seismic source to obtain the subsurface structure in the area around the quarry. We designed a straight line along the State Route 7, for total of 7455m, and deployed 72 Fairfield 3 component nodes in a temporary dense linear array with 105m spacing, where the first node on the West side of the array is 120m to the quarry site. In order to capture more than one quarry blast for comparison of the similarity of the source, the acquisition period lasted for 28 days between April 15th to May 11th ,2018. However, during the period, the 12th geophone in the array was malfunctioned, thus, there is no data recorded at this location. The node we use is board band geophone with the sampling frequency of 500Hz, the sensitivity is 12dB, and data is recorded hourly. During the 28 days period, we have been informed that there were three blasts in total, and the time precision is in minute which allows us to find the blast directly in records among the deployment period. During the 28 deployed period , we requested and received the time of each blast, which are: 13:22 April 17th , 15:30 April 26th ,and 16:00 May 7th. However, the exact excite time of each blast is unknown, hence we extract the total of 30 second data, in our record, and 0.5 second prior to the onset time of the first geophone, and the onset time is where the first receiver initially captures the signal of the quarry blast and shows the tendency of wave propagation to the further geophones.

The raw normalized shot gathers recorded in UD-component for each blast is shown in figure 2, where each trace is normalized according to the absolute maximum among all the traces in the each gather, the missing trace is caused by the malfunction of 12th geophone. Additionally, since we don’t have the knowledge of each source’s excitation time and location, we put the onset time at 0 seconds for each gather that indicates where the first receiver in the array first captures the

quarry blast signal. Notice that the third blast on May 7th has the highest amplitude and signal to noise ratio, and the shot gather from the other two components are also displayed in figure 3(a) and (b). We mainly focus on processing the signal recorded from the third blast due to this relatively high signal to noise ratio.

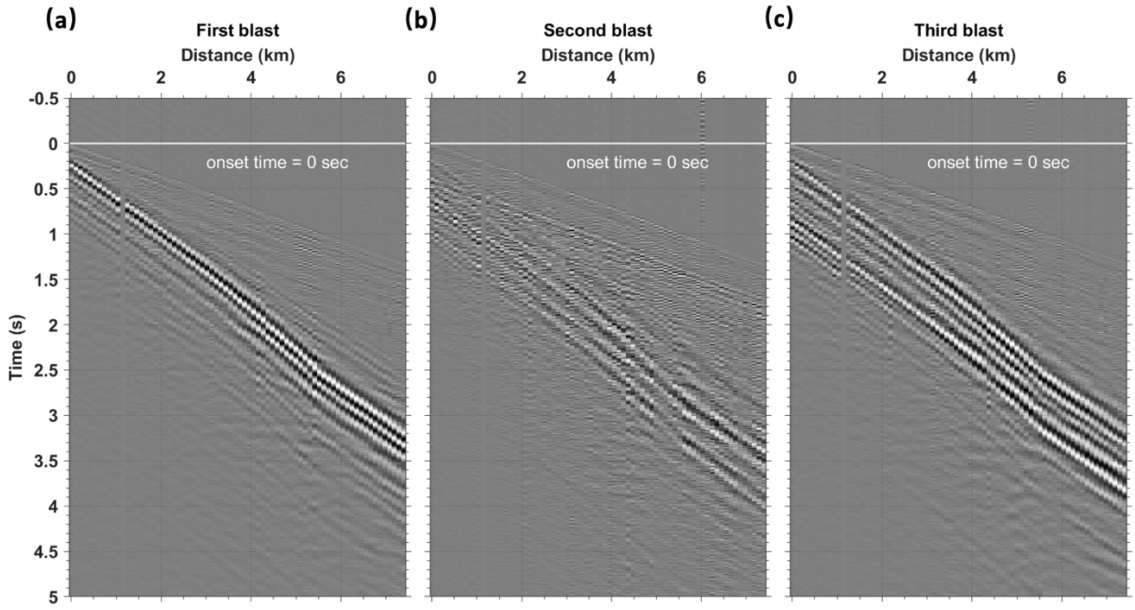

Figure 2: Raw shot gathers of each blast in the Z component. The onset time, which is estimated below, is set to be 0 second in each panel. The distance origin is the first receiver used. Amplitudes of each panel are normalized according to their absolute maximum among all traces in the panel. The blast time are at: (a)13:22, 17 April 18; (b) 15:30 26 April 2018; and (c)16:00 7 May 2018 in CDT, respectively.

Chapter 3: Observed seismic waves

3.1 Frequency spectra

To evaluate the predominant frequency and energy level of the quarry blast signal, we compute the power spectra for time windows that include the blast and back-ground noise (Jana et al. 2017). The power spectral density analysis decomposes the signal recorded in the time domain into different sinusoidal waves with different frequencies and amplitudes by Fourier transform (Cooley and Tukey 1965), hence we can observe the predominant frequencies for each blast and each component by comparing the ambient noise power spectrum, and then use suitable frequency range to further enhance the signal to noise ratio by applying the bandpass filter.

Since we snipped 30-seconds of data for each shot gather, for a better comparison, we need to keep the same duration for our noises, and comprehensively describe the ambient noise. Therefore, we choose the 1-hour signal recorded in EW, NS, and UD components that is 24 hours prior to the blast time for each shot as a background noise and compute the power spectrum for every 30-second time window within that 1-hour record without any overlap, and then averaged all of it as our background noise power spectrum. For the purpose of comparison, we normalized the power spectra for all blasts and background noise recorded in each component with maximum value of the background noise power spectrum.

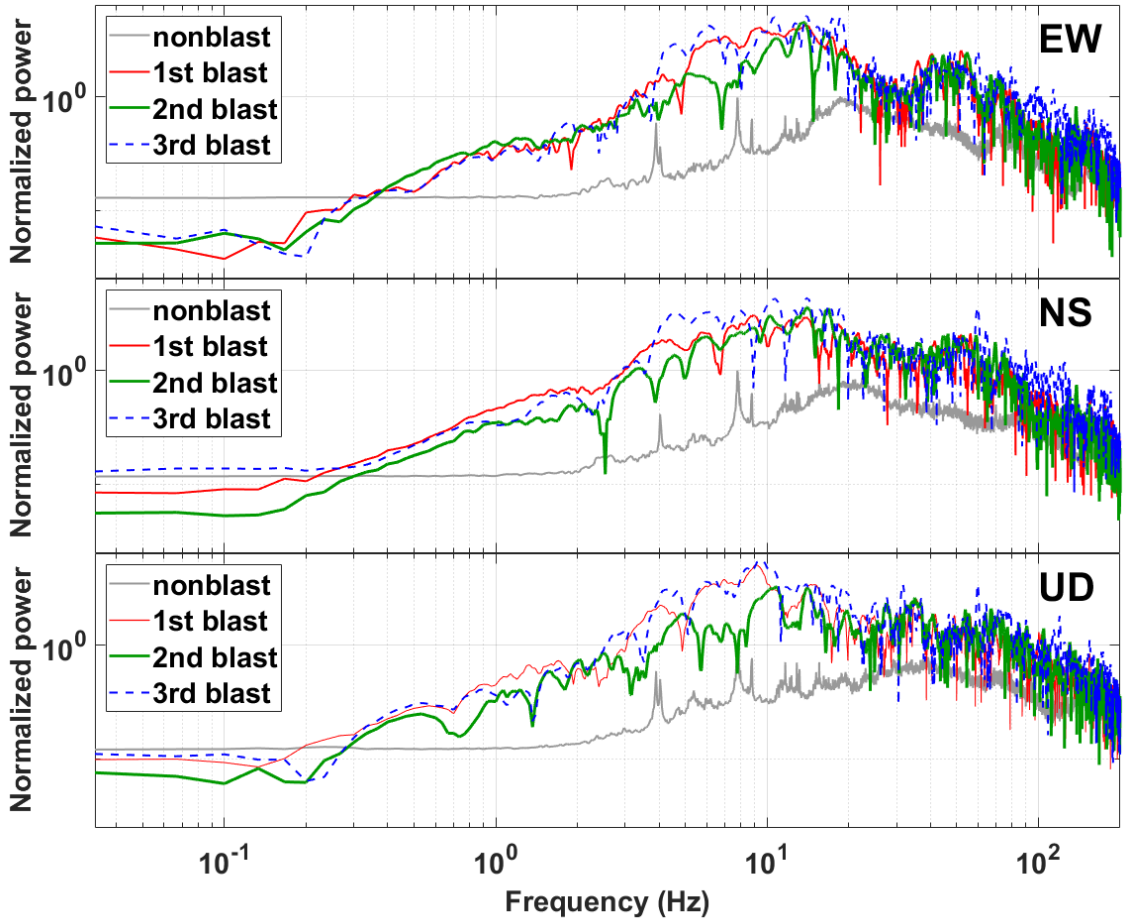

Figure 3: The normalized power spectra of a 30 second time window from onset time for all three shots that recorded from the first receiver. Each panel from top to bottom represents the east component, north component, and vertical component respectively. The gray line represents the power spectrum of a 30 second time window of back ground noise 24 hours prior to the 3rd blasting time. Each spectrum in different component is normalized based on the maximum power of the noise.

The result is shown in figure 3, from top to bottom are EW, NS, and UD components respectively, for each blast. In order to observe the signal's dominant frequency, we plot the power density spectra in log-log scale. We observe that the predominant frequency range for each component and each shot is between 4Hz and 20Hz, and by comparing with the power spectrum of background noise to depict the signal from the ambient noise, we observe that it covers a quite large range: 0.5Hz to 80Hz. Other studies also observe that quarry blasts have low-frequency (Allmann, et al, 2008; Baumgadt 1995), and the cause of this low frequency as Allmann et

al.(2008) explained, could be due to ripple excitation of the source or the strong near-surface attenuation.

3.2 Energy level of the blasts

The evaluation of the energy level for different blasts is essential information for using quarry blast as an active seismic source as well. Normally, the shot gather is common shot point gather due to some logistics, thus, knowing the energy level will help to estimate the size of the array by knowing the valid propagation distance, also to ensure that the energy is enough to penetrate deep enough to obtain the structural response and can be recorded by the geophone.

Power spectral density analysis also provides an insight of the energy level for each blast. From figure 3, we also observe that the power for the third blast among all components are the strongest, which is 10^3 times stronger than the power of background noise, we also notice that for the frequency that is lower than the predominant frequency range, the energy level is not highest among all the blast. The First blast has slightly lower energy level within the predominant frequency range compared to the third blast, whereas the second blast has the smallest energy level among all the blasts in all component. Therefore, since we can capture the weakest quarry blast from the furthest receivers, that is more than 7km is away, then the blast contains enough energy to propagate far enough to be captured by receiver.

3.3 Similarity of shot gather

The similarity of the shot gather can reflect whether the source wavelet and temporal local geological change during the deployment period. Since the amount of dynamite used for blast is unknown, we can use the energy level and the time duration of the wave package to estimate. The shot gather for all three blasts recoded at UD-component shown in Figure 2; we use a total of 5.5 second time length to display the shot gathers, since after 5 second, there are nothing can be

observed from the gather. Time starts 0.5 second earlier prior to the onset time that represented by line in the figure.

We observe that for all three blasts, the wave propagation patterns are similar to each other. The pattern observed: the decrease of the slope from 4.4km to 5.4km indicates a velocity decrease, and an increasing of slope beyond 5.4km. Additionally, the slope of P wave is constant via distance, thus, there is no change in the local geology with 28 days of deployment. Given this velocity decrease among the first arrival, we cannot implement the refraction survey, since it needs a sharp velocity contrast, and the trend of the velocity should be increased, otherwise, according to Snell's law, the wave will dive to deeper subsurface.

3.4 wave type Identification

It is necessary to separate the P waves and S wave in order to understand the velocity for each wave to estimate the origin time and distance for each blast, and furthermore we can apply the imaging conditions such as elastic Helmholtz wave mode decomposition(Zhu 2017), accorded by Figure 4 shows the normalized shot gather among the third shot, EW, NS, and UD components. Each gather is normalized based on absolute maximum value in all traces. Since the Martin Marietta quarry is located to the west side relative to our geophone line, thus we expect to observe the P wave in UD-component, and S wave in horizontal components, especially, SH along NS component and SV associated with UD and EW component. In order to depict the P wave, we apply the bandpass filter to the UD component with frequency range of 0.3-1Hz, 4-8Hz, and 8-24Hz that is illustrated in figure 5. We observe that in the frequency range of 0.3-1Hz, and 4-8Hz, the S wave has a higher energy level compared to the P wave, this suggest is the frequency range to identify S wave is relatively low. Since 4-8Hz frequency range provides a relatively clear S wave pattern, we kept this frequency range for particle motion analysis to differentiate SH and SV wave. Furthermore, we observe the existence of air wave in our shot gather for a bandpass range

between 0.3Hz to 1Hz with a square time gain, which is useful in estimation of the origin time and distance of the source.

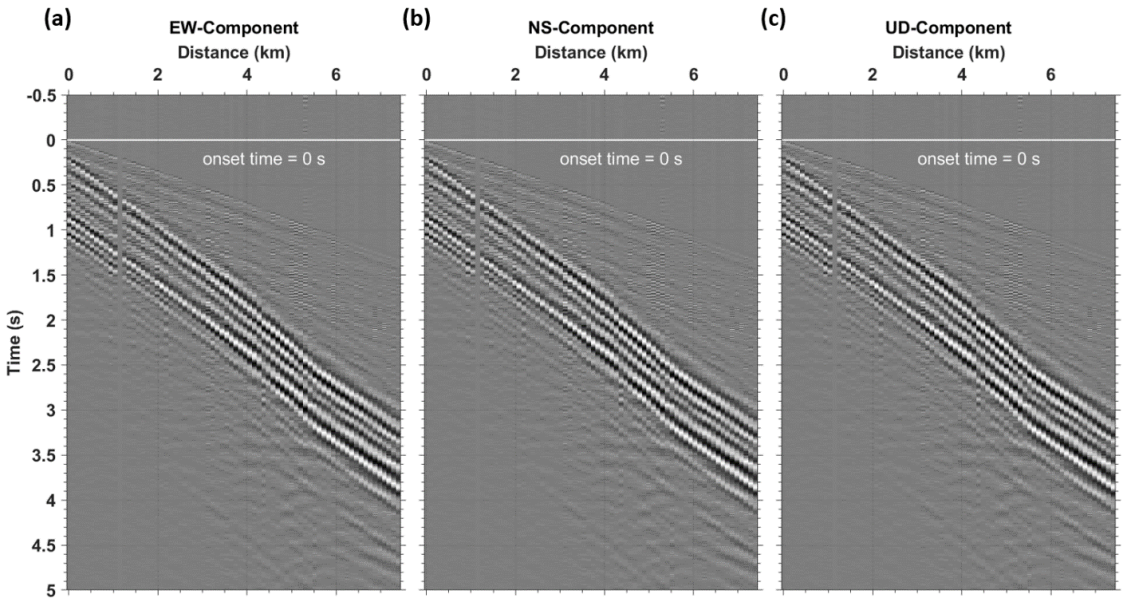

Figure 4: Third blast shot gathers in each component without bandpass filters. The onset time in each panel is set to be 0 second as estimated below. The distance origin is the first receiver used. Amplitude of each panel are normalized according to their absolute maximum among all traces in the panel. (a) EW-component, (b) NS-component, and (c) UD-component.

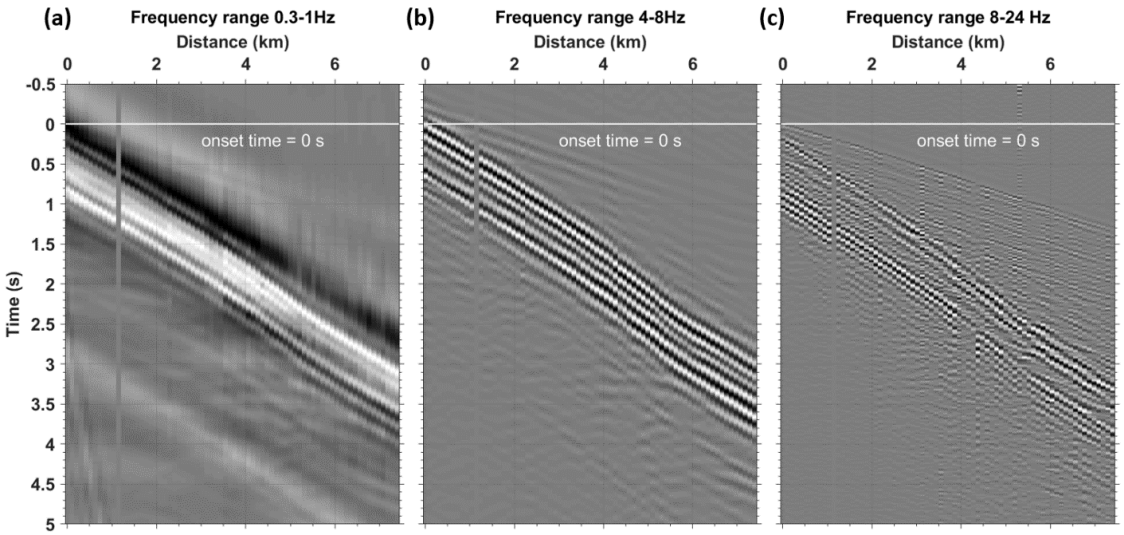

Figure 5 : Band-pass and normalized shot gathers of third blast, UD component in different frequency range. From left to right: (a) 0.3-1Hz, (b) 4-8Hz, (c)and 8-24Hz respectively. since the change of the wave trains arrival are the same in different frequency range i.e. not dispersive, we consider that there is no surface wave. The S-wave is marked with higher normalized amplitude in a 0.3-1Hz and 4-8Hz, where the P-wave requires broader band to recover, which shown clearer in 8-24Hz frequency band.

3.4.1 P wave identification

In active seismic imaging, the P wave is the most important part, especially for migration in a reflection survey and first arrival time analysis in a refraction survey. However, normally for a quarry blast, it's not frequent to record for single shot (non-delay shot), which preserves the P wave the best way, instead, it's often shot in ripple firing fashion, that results in strong attenuation.

We observe the P wave better in a frequency range from 8 to 24Hz in figure 5, which is a relatively broader range compared to the S wave. Where the P wave shows a more consistent slope as it propagates to the furthest geophone, this suggest a relative homogeneous medium in the subsurface since the velocity for P wave is almost constant. Additionally, this constant velocity constrains us to implement the refraction survey, due to lack of sharp velocity change.

3.4.2 Air wave identification

While investigating the shot gather, we found the existence of the air wave in UD component among all blasts. Figure 6 shows the shot gather for the UD component with the frequency range of 0.3 to 1Hz for the third blast. To better isolate of the appearance of the air wave, we use the time squared gain. In this figure, we observed a wave train from 2 seconds to 25seconds, and by estimating the slope, we know the velocity is around 350m/s, which is the speed of sound. With the existence of the air wave, we can then further restrict of the error of time and distance estimation.

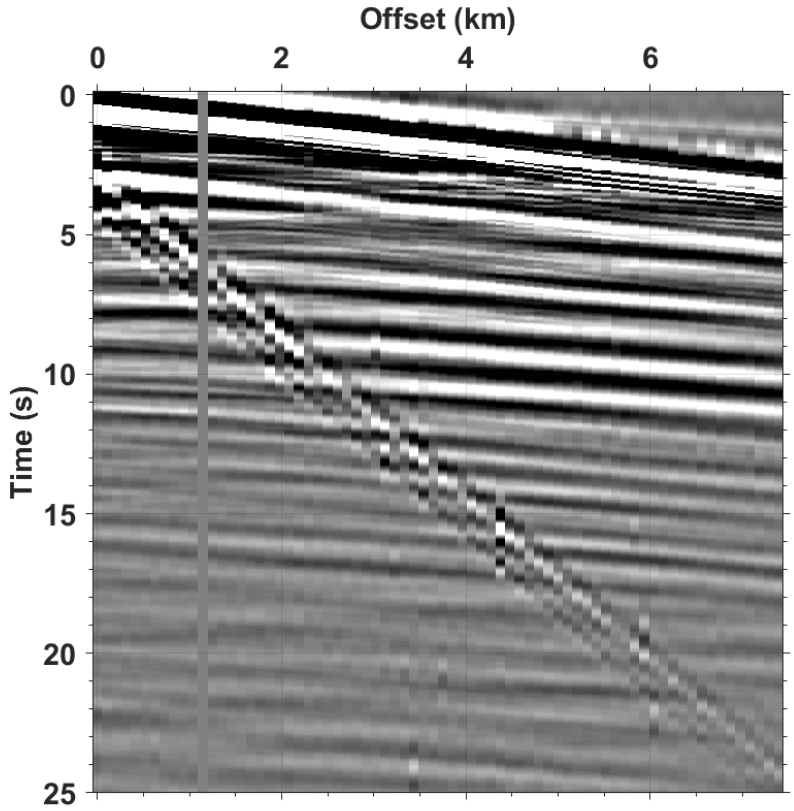

Figure 6: A squared time gain for 0.3-1Hz frequency band shown in figure 5. The linear, longer time duration wave train from time 2.5sec to 25sec is the air wave from the blast.

3.4.3 SH and SV wave identification

For the identification of SH and SV wave, we adopt a particle motion analysis. Given the location of the quarry and the geometry of our geophone line, by performing such a method, we can show the correlation between the UD component and EW component, whereas the NS-component is independent and SH wave predominant. As figure 7 shows, we use 1 second time window that starts from the first S-wave observation in each trace from NS, EW, and UD component. The color shows the particle motion for a second time window. The representative traces selected are 20^{th}, 40^{th} , and 60^{th} trace to observe the change in the orientation of the motion as the energy propagates further.

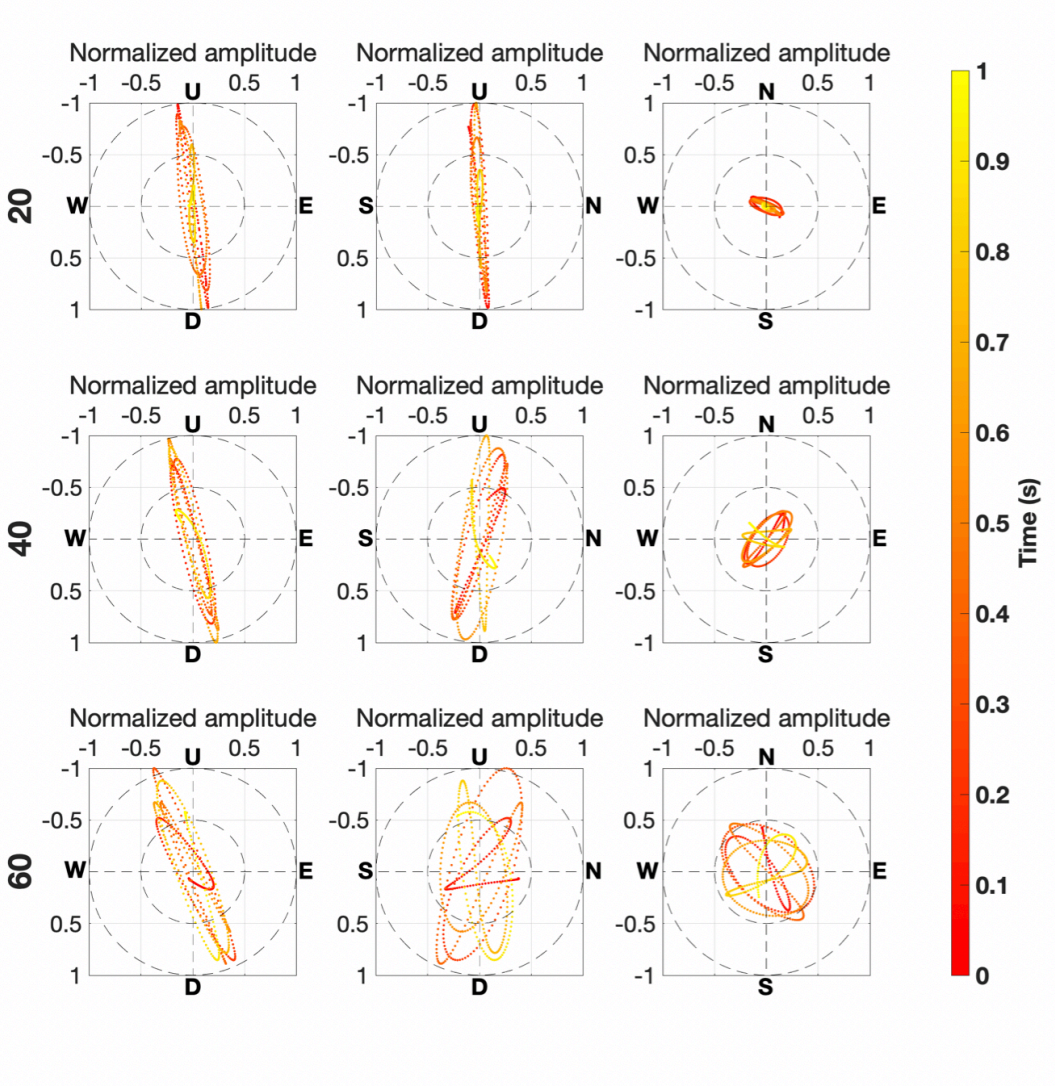

Figure 7 : Particle motion analysis for shear wave within 1sec from where the shear wave first recorded, for receiver 20th, 40th, and 60th receiver, third blast. As the figure shows, the SV wave is associated with EW and UD component since the orientation of orbit is changing as the incident angle of ray path decrease, where the SH wave is independent, and associate only with NS component.

The orbit of particle movement for SH wave is perpendicular to the plane that describes the ray path between the source and receiver. Due to the spherical spreading effect that occurs as wave propagates to longer distances, the orbit for the particle motion is more dispersed. By looking the particle motion analysis for NS component and UD component, and incorporating with the

geometry, we discovered that the SH wave is independent to the UD component, since there is no direct relation of the incidence angle of ray path and orbit orientation.

The orbit orientation for SV wave particle movement is perpendicular to the ray path between the source and receiver. As the incidence angle of the ray path decrease with increasing distance, the orientation for the SV wave should change in an inverse relationship since the P-wave particle motion is along the ray path, and the SV is perpendicular to the P-wave's particle motion. We can also observe this in the left panel of figure 7. The particle motion analysis confirms that SV wave is associated with UD and EW component, where SH wave is independently recorded in the NS component.

3.5 Origin time and distance

To estimate the true source distance and the origin time for each blast, since the P, S, and air waves are relatively linear, we can use the semblance analysis for P, S, and air wave in each blast. The procedure is to sum the amplitude in the gather along the wave is defined by the velocity, and zero-offset travel time, and then the semblance gather maximum is picked, which is the root mean square velocity. The semblance analysis results are shown in figure 8, where the analysis for P, S, and air waves from left to right respectively. We assume that all the waves are generated by the same source and travels the same distance, hence, we can solve for the origin time in following way:

$$V_{air} * \left(t_{origin} + t_{air}\right) = V_s * \left(t_{origin} + t_s\right) = V_p * \left(t_{origin} + t_p\right)$$

Where t_{air}, t_s, t_p and V_{air}, V_s, V_p can be obtained from semblance analysis. So that we have three equations to solve for 1 unknown: t_{origin}. Thus, we obtain three t_{origin} after the calculation, and then we take mean of all three t_{origin}, and set as the origin time for each blast. Finally, we plug the t_{origin} back to equation and estimate the distance between source and first receiver. The result shows in table 1.

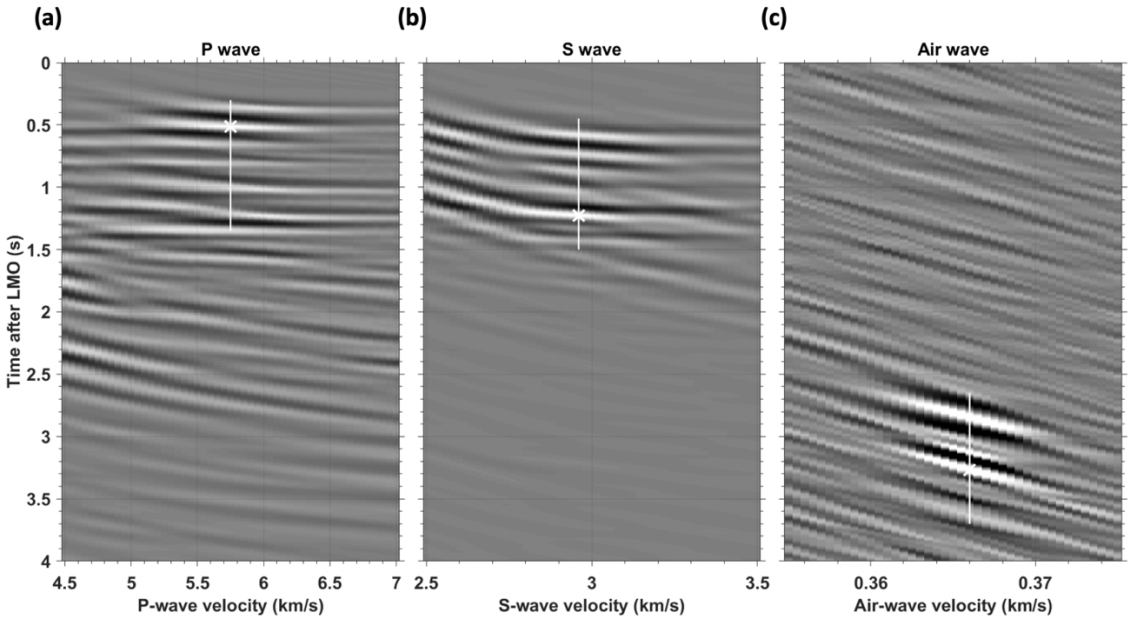

Figure 8 : The semblance analysis for the third blast. The white line indicates the 1.05sec energy duration for each wave in this blast, and the star indicates maximum root mean square velocity. Since all the wave are generated from a same source location, hence, we can calculate the source distance with this velocity, and furthermore, depict the origin time prior to the onset time. Semblance analysis shows for P, S, and air wave are shown in (a), (b), and (c) respectively, and origin time and distance are documented in table 1.

	Origin time prior to onset time(sec)	***Origin distance from receiver 14(km)***	***P-wave velocity (km/s)***	***S-wave velocity (km/s)***	***Air wave velocity (km/s)***
Blast 1	0.254	1.053	6	2.9	0.359
Blast 2	0.3902	0.9656	5.95	2.98	0.375
Blast 3	0.141	0.919	5.75	2.96	0.366

Table 1: Semblance results for three blasts from April to May 2018, total of 71 sensors are used (1 sensor is malfunction during the time).

Chapter 4: Discussion

4.1 Velocity variation and subsurface structure

From figures 2,3, and 5, we observe that there is a velocity decrease between offset distances 4km to 6km. To confirm if this is caused by the local geology, we use first order central finite difference with forth order error estimatiom to calculate the shear wave velocity at each geophone location, for all blasts and all components, and the equation shown below:

$$F'(x) = \frac{-F(x+2h) + 8F(x+h) - 8F(x-h) + F(x-2h)}{12h}$$

As figure 9 shows, for all blast, the S-wave velocity recorded in NS-component is faster than the S-wave recorded in EW and UD Component. Additionally, we find that for all components in all three blasts, the velocity drops between 4 km to 5.2 km, and increase after 5.2 km. Since it is observed in all blasts, then it must be associates with the geology. From figure 1, a mapped strike slip fault that cut through our receiver lines at 5.4km (52th receiver) there is possibility that at 4km, there is an unmapped fault, branches out from the big fault and intersect the receiver line at 4km. Hence, in between 4km to 6km, there is a fault damage zone, and from 5.2km to 5.6km could be the core damaged zone.

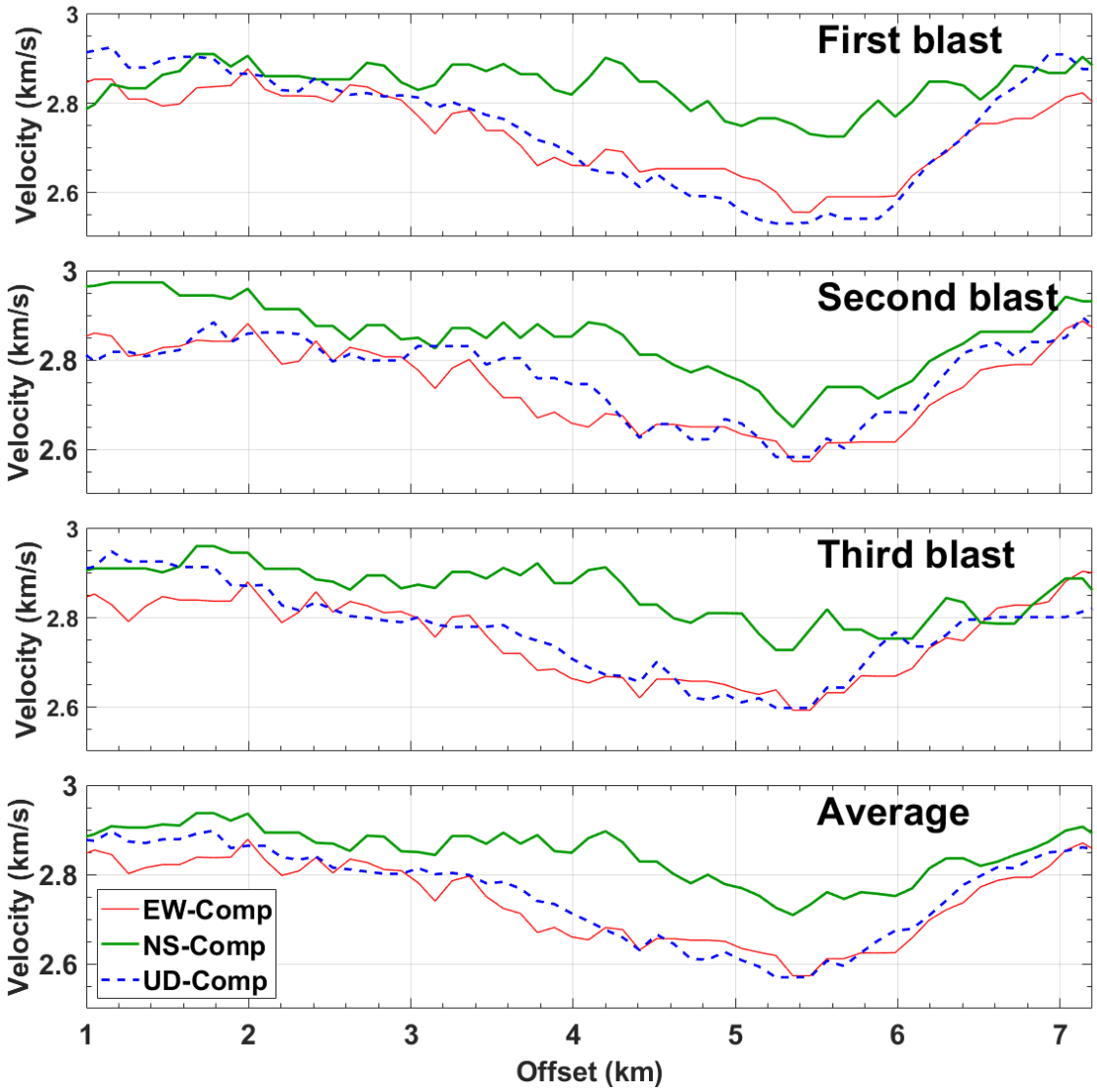

Figure 9 : Calculation of phase velocity at each receiver for all blasts and all components using first derivative finite difference calculation with 4th order estimation. Top three panel indicates the results for each component at each blast, last one is the mean of all blasts for each component. lack, which indicates that the subsurface geological consistency during the deploy time. We interpret that the change between 4km to 6km is due to a damage zone due to a mapped fault at 5.4km (52th receiver).

4.2 Attenuation

Understanding the attenuation as a function of distance can help us to better design the geometry of the receiver line to properly utilize the quarry blast signal. As shown in figure 10, the black line indicates the normalized power spectrum for first receiver based on its maximum, and the red line is the normalized power spectrum based on the same maximum value for the 10th, 40th, and 70th receiver's power spectrum for each component from the third blast. The distances from the source location to the selected receiver locations are: 1924m, 5074m, and 8224m respectively. Hence, from the figure, we can not only observe that the energy level is decreasing relative to the level at 1st receiver, which is 980m away from the source.

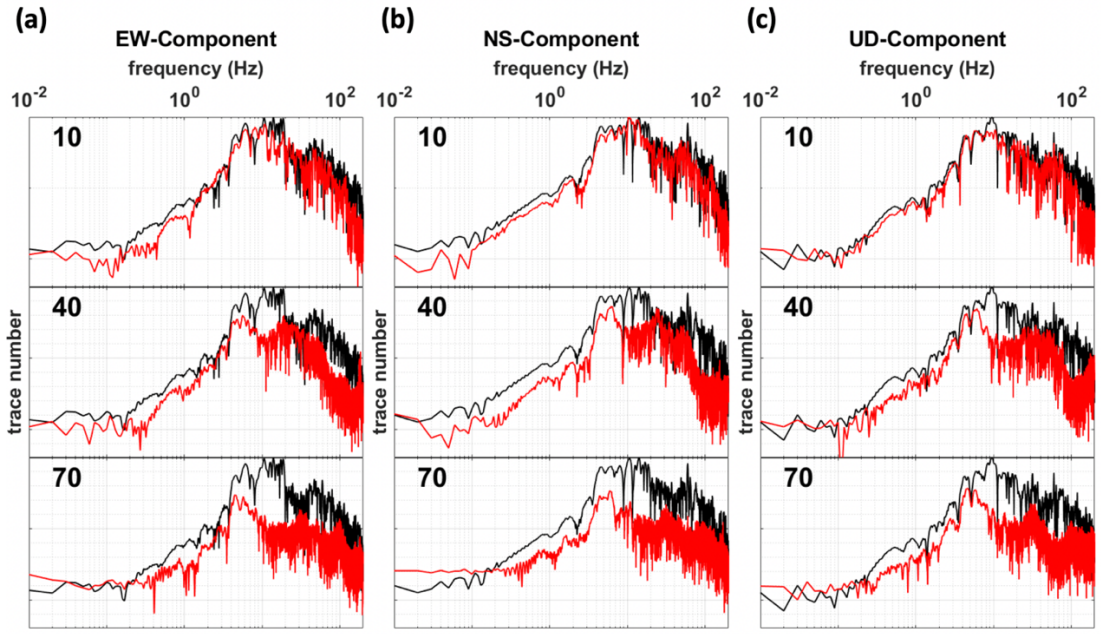

Figure 10 : Power spectra for 1st ,10th, 40th, and 70th receiver from EW, NS, and UD component in blast 3 shown in figure 10 (a), (b), and (c). In each panel, the black line is the power spectrum from first blast, and the red line is the power spectrum corresponding to the receiver number annotated on each figure. According to the distance from calculated source location to receiver, and the percentage of energy preserved, we found that the loss of energy is a function of distance and the gradient is 1% for every 126m.

4.3 Lack of reflection

Based on the shot gathers we observed, we did not find any reflected waves in the gathers. We interpreted this is because of the homogeneity of the subsurface material. From figure 1(a).

The geology where we set the geophone array is above a homogenous granite, with the dyke and sill intrusions which mainly composed of diabase. From the lab measurements, the granite velocity ranges from 5.5-6km/s and diabase from 5.8-6.3km/s (Kolawole, personal communication). Therefore, the velocity contrast is very small, which is hard to create a reflected wave. In order to have a reflected wave, the velocities for two layers would need to have some amount degree of variation, i.e. first layer has to have slower velocity than the second layer. Due to the difference of P wave velocity between different rocks are relatively small, which means the impedance contrast is small, we hence conclude that the reason we could not observe the reflected waves in the shot gather is because of it. Additionally, from the size of the dike exposed on surface is less than 1m, and the size of the sill is from 5 to 10 m, hence the resolution could also not depict those characters as well.

Chapter 5: Conclusion

Anthropogenic active sources can be used to understand and image the subsurface with calculated origin time and distance. In this paper, we show an example of using explosive source for quarrying purpose to acquire subsurface information. Even without the reflected waves, we are still able to characterize and interpret the near-surface geology by using direct waves incorporates with a finite difference method. The occurrence of the air wave provides us a constraint to estimate the source origin, time, and location, which is necessary information to treat an anthropogenic source as active source to image the subsurface. The frequency range for mining blast is broad, but the predominant frequency range is small and low compared to the frequency range for active source imaging. Thus, the frequency range selection needs to be small.

We incorporate with the finite difference estimation, and calculate the velocity at each receiver position, and found that between 4 to 6km in our receiver array, there is a gradually velocity decrease, which we interpret as damage related to a mapped fault at 4km to a known fault at 6km. Additionally, the reason of the lacking the reflection is due to a small velocity contrast between the granite and diabase intrusion, also the size of the intrusion is very small as well.

Reference

Allmann, Bettina P., Peter M. Shearer, and Egill Hauksson. 2008. “Spectral Discrimination between Quarry Blasts and Earthquakes in Southern California.” *Bulletin of the Seismological Society of America* 98(4):2073–79.

Baumgadt, Douglas R. 1995. “CASE STUDIES OF SEISMIC DISCRIMINATION Directorate of Geophysics.”

Berkhout, A. J. Guus and D. J. Eric Verschuur. 2011. “A Scientific Framework for Active and Passive Seismic Imaging, with Applications to Blended Data and Micro-Earthquake Responses.” *Geophysical Journal International* 184(2):777–92.

Bickford, M. E., W. R. Van Schmus, K. E. Karlstrom, P. A. Mueller, and G. D. Kamenov. 2015. “Mesoproterozoic-Trans-Laurentian Magmatism: A Synthesis of Continent-Wide Age Distributions, New SIMS U-Pb Ages, Zircon Saturation Temperatures, and Hf and Nd Isotopic Compositions.” *Precambrian Research* 265:286–312.

Brewer, J. A., R. Good, J. E. Oliver, L. D. Brown, and S. Kaufman. 1983. “COCORP Profiling across the Southern Oklahoma Aulacogen: Overthrusting of the Wichita Mountains and Compression within the Anadarko Basin.” *Geology* 11(2):109–14.

Cooley, James W. and John W. Tukey. 1965. “An Algorithm for the Machine Calculation of Complex Fourier Series Published by : American Mathematical Society Stable URL : Http://Www.Jstor.Org/Stable/2003354 REFERENCES Linked References Are Available on JSTOR for This Article : An Algorithm for the Ma.” 19(90):297–301.

Fereidoni, Azadeh and Gail M. Atkinson. 2017. “Discriminating Earthquakes from Quarry Blasts Based on Shakemap Ground-Motion Parameters.” *Bulletin of the Seismological Society of America* 107(4):1931–39.

Jana, Niptika, Chandrani Singh, Rahul Biswas, Nitin Grewal, and Arun Singh. 2017. “Seismic

Noise Analysis of Broadband Stations in the Eastern Ghat Mobile Belt of India Using Power Spectral Density." *Geomatics, Natural Hazards and Risk* 8(2):1622–30.

Kolawole, Folarin et al. 2018. "CHARACTERIZATION OF PRE-EXISTING STRUCTURES IN THE BASEMENT OF OKLAHOMA WITH IMPLICATIONS FOR INDUCED SEISMICITY." (158–6).

Li, Baolin et al. 2017. "Discriminant Model of Coal Mining Microseismic and Blasting Signals Based on Waveform Characteristics." *Shock and Vibration* 2017.

Li, Guanglei et al. 2017. "An Electrochemical, Low-Frequency Seismic Micro-Sensor Based on MEMS with a Force-Balanced Feedback System." *Sensors (Switzerland)* 17(9).

Nakata, Norimitsu, Roel Snieder, Takeshi Tsuji, Ken Larner, and Toshifumi Matsuoka. 2011. "Shear Wave Imaging from Traffic Noise Using Seismic Interferometry by Cross-Coherence." *Geophysics* 76(6):SA97-SA106.

Quiros, Diego A., Larry D. Brown, and Doyeon Kim. 2016. "Seismic Interferometry of Railroad Induced Ground Motions: Body and Surface Wave Imaging." *Geophysical Journal International* 205(1):301–13.

Reshetnikov, A., S. Buske, and S. A. Shapiro. 2010. "Seismic Imaging Using Microseismic Events: Results from the San Andreas Fault System at SAFOD." *Journal of Geophysical Research: Solid Earth* 115(12):1–9.

Shashidhar, D., K. Mallika, N. Purnachandra Rao, H. V. S. Satyanarayana, and H. K. Gupta. 2014. "Detection of Quarry Blasts in the Koyna-Warna Region , Western India." (November):162–69.

Smith, B. Y. Albert T. 1993. "Mining Blasts." *Society* 83(1):160–79.

Xu, Zhuo et al. 2012. "Reconstruction of Subsurface Structure from Ambient Seismic Noise: An Example from Ketzin, Germany." *Geophysical Journal International* 189(2):1085–1102.

Yilmaz, Şeyda, Yusuf Bayrak, and Hakan Çinar. 2013. "Discrimination of Earthquakes and Quarry Blasts in the Eastern Black Sea Region of Turkey." *Journal of Seismology* 17(2):721–34.

Zhu, Hejun. 2017. "Elastic Wavefield Separation Based on the Helmholtz Decomposition." *Geophysics* 82(2):S173–83.

Appendix A: 2D grid receiver array processing

In order to verify the validity of our proposed workflow and test the robustness with a different receiver geometry setting, we deployed 30 sensors from February to March in 2018 in an off-road park, which located 4.5km southeast of the quarry site as shows in figure 11. The blue pin is each receiver location, and the yellow pin indicates the location of the quarry site.

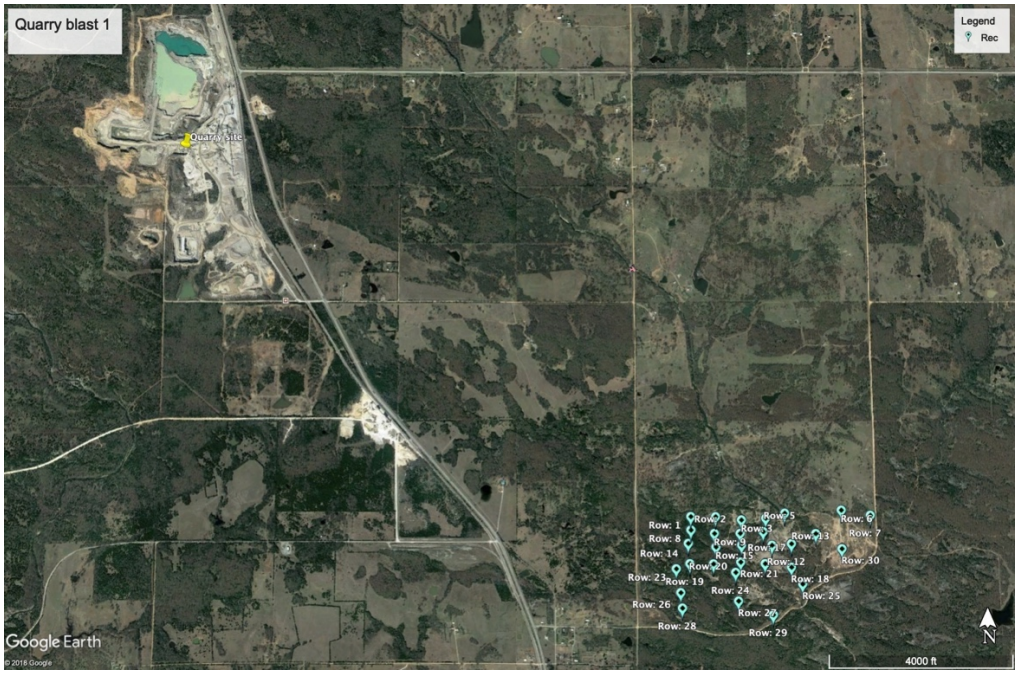

Figure 11: Indicates the study area of introduced in the appendix, where the yellow pin is where the quarry site located, and the blue pin is the receiver location.

We were informed from company that during the deployment time, there are 3 blasts, with the shot gathers displayed in Figure 12. The distance is the first receiver (top, left one in the array) to the origin blast location computed from semblance test. The onset time 0 seconds indicates where the first receiver (spatially) first recorded the wave. Shot gather from March 5th actually recorded the

reflected waves from moho, at time 11seconds.

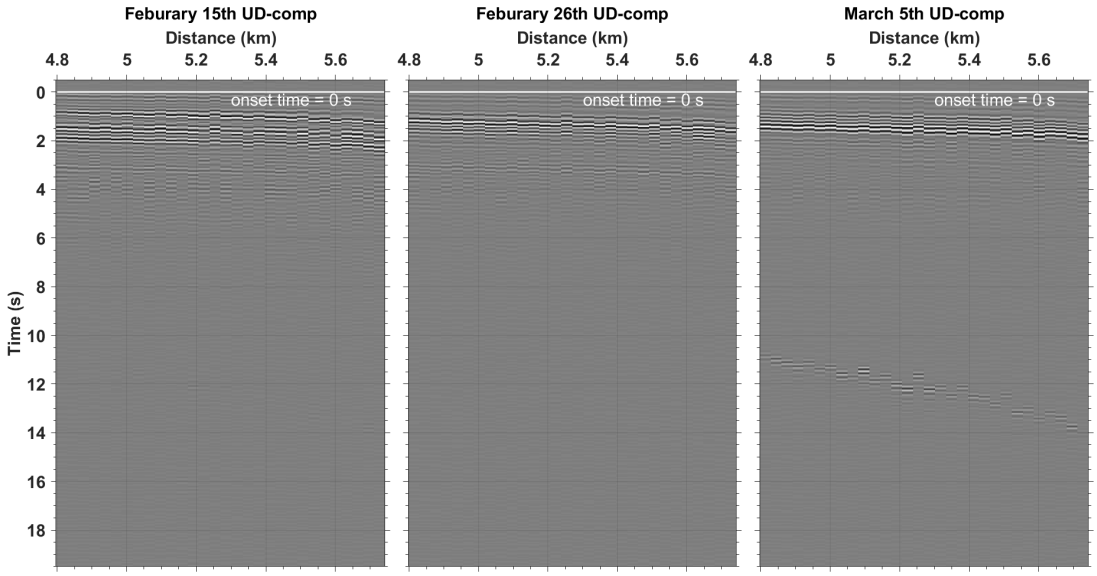

Figure 12: Shot gathers of each blast in the UD component with band pass filter of 4 to 8Hz. The onset time, which is estimated below, is set to be 0 second in each panel. The distance origin is the first receiver to the blast location obtained from semblance analysis. Amplitudes of each panel are normalized according to their absolute maximum among all traces in the panel. The blast time are at: (a)14:35, 17th February 2018; (b) 12:09 26 February 2018; and (c)16:08 7 March 2018 in CDT, respectively.

We also use the frequency spectral analysis for the spatially closest receiver to find the dominant frequency range shows in figure 13, and the computation follows exactly the same as we did for the receiver line in main content. The dominant frequency shifts to higher range: 40 to 70Hz. However, there is second dominant frequency range: 2 to 10 Hz, this is because the distance is further, hence, the lower frequency wave attenuates more compared to the higher frequency waves.

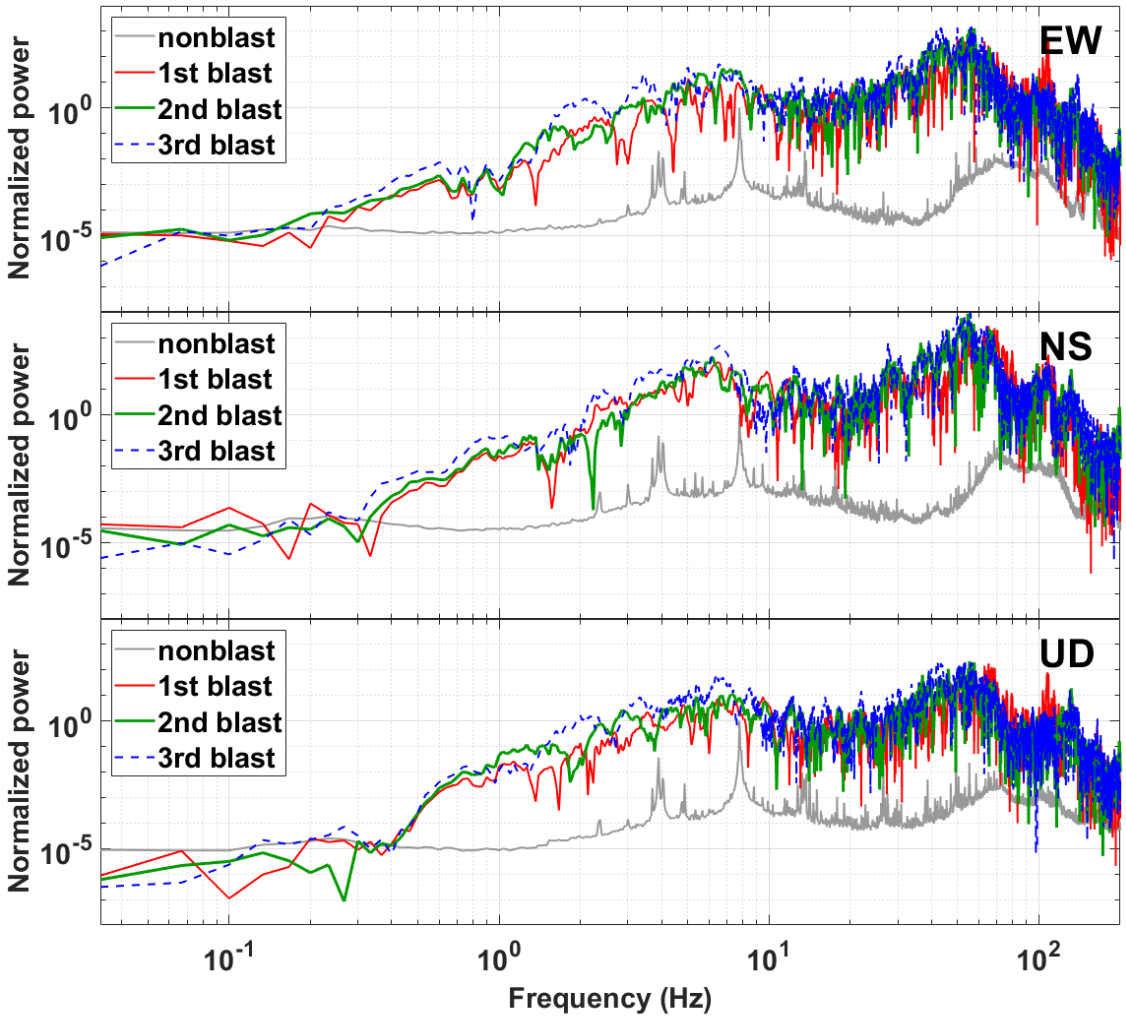

Figure 13: The normalized power spectra of a 30 second time window from onset time for all three shots that recorded from the first receiver. Each panel from top to bottom represents the east component, north component, and vertical component respectively. The gray line represents the power spectrum of a 30 second time window of back ground noise 24 hours prior to the 3rd blasting time. Each spectrum in different component is normalized based on the maximum power of the noise.

Due to the occurrence of an air wave from the blast on March 5th, we did a more detailed analysis for this blast, and the shot gathers for all three components are shown in figure 14. We observe that the air wave in the UD component is much stronger than other two components, since it's a type of a compressional wave.

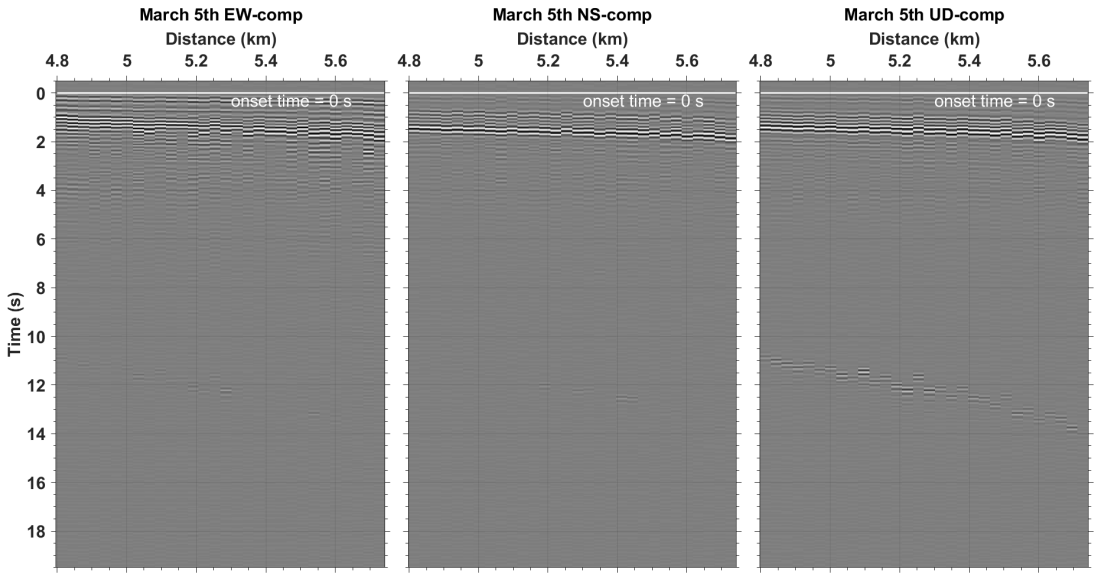

Figure 14: Third blast shot gathers in each component without any bandpass filters. The onset time in each panel is set to be 0 second as estimated below. The distance origin is the first receiver to the blast location obtained from semblance analysis. Amplitude of each panel are normalized according to their absolute maximum among all traces in the panel. (a) EW-component, (b) NS-component, and (c) UD-component.

We then use the same bandpass frequency ranges as we did in main content to identify the wave type. We still explore the air wave in a much lower frequency range: 0.3 to 1Hz, and a clear P and S wave pattern shows in frequency range of 4 to 8Hz. However, for higher frequency range, the shot gather is much noisier, we cannot tell too much from it. Additionally, in order to have a better view of the air wave, we also incorporate the squared time gain, with the frequency range of 0.3 to 1Hz, and the result is shown in Figure 16. Since the arrival time of receiver at 4.8km is 11 seconds, and the arrival time for receiver at 5.7km is 13.5 seconds, thus, the velocity is 0.37km/s, also given that the linear trend of this wave train, we can exclude the possibility of this wave pattern as reflected waves from moho.

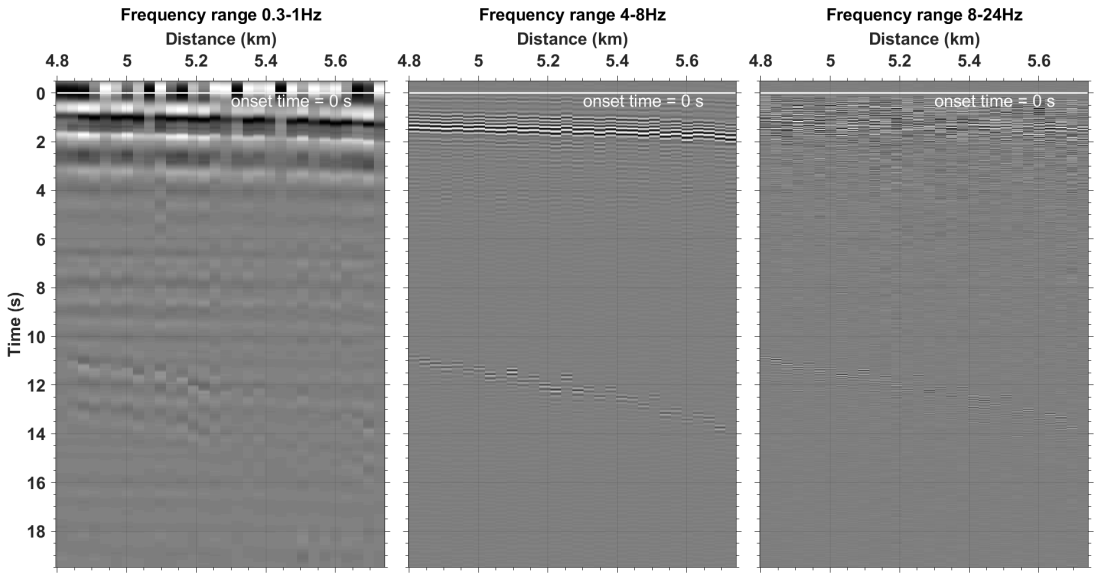

Figure 15: Band-pass and normalized shot gathers of third blast, UD component in different frequency range. From left to right: (a) 0.3-1Hz, (b) 4-8Hz, (c)and 8-24Hz respectively. since the change of the wave trains arrival are the same in different frequency range i.e. not dispersive, we consider that there is no surface wave. The S-wave is marked with higher normalized amplitude in a 0.3-1Hz and 4-8Hz, where the P-wave requires broader band to recover, which shown clearer in 8-24Hz frequency band.

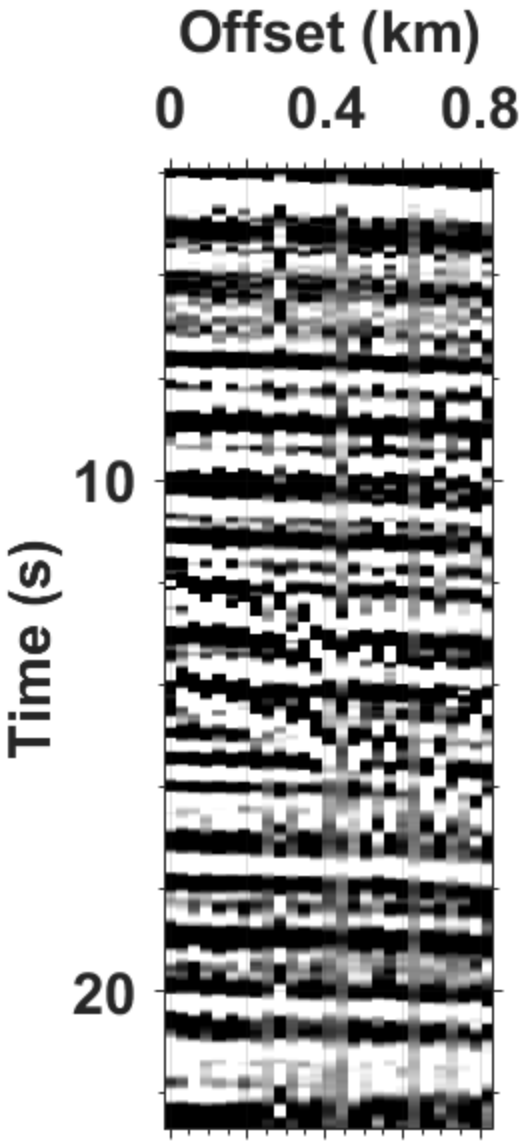

Figure 16: A squared time gain for 0.3-1Hz frequency band shown in figure 5. The linear, longer time duration wave train from time 11sec to 13.5sec is the air wave from the blast.

For estimation of the source origin location and time, we incorporate not only the semblance analysis, but also taking advantage the receiver array processing approach, beamforming. Beamforming is an approach that uses a sensor array to find the direction of the energy transmission and reception.

Here, from the semblance analysis for each blast, we found that the P-wave velocity from 5.5km/s to 5.2km/s, and shear wave velocity varies from 2.84 km/s to 2.58km/s, air wave velocity is relatively consistent, has the magnitude of 0.37km/s. The semblance result for each blast (from blast 1 to blast 3) are illustrated from figure 17 to figure 19 respectively, the semblance results for each blast are shown in table 2.

For beamforming, we analyze the P-wave and S-wave separately, in order to confirm the velocity. The P-wave result from beamforming for each blast is represented in figures 20, 21, and 22. The circle represents a velocity, the most inner circle has a velocity of 10km/s, the second outer circle represents the velocity of 5km/s, and the most outer circle represents a velocity of 3.33km/s. The result from beamforming for shear wave are shown in figures 23 to 25, and the most outer circle represents a velocity of 2.5km/s. The results show a very consistent direction of wave propagation for both P and S wave. The brightest spots indicate the azimuthal direction, and the color intensity indicates the energy level of wave, the location of the hotspot indicates the direction, and also the velocity. Therefore, for both P and S wave, the energy come from the 315 to 318 degrees azimuthally, where the 0 degrees is the North, therefore, the waves are from northwest of the receiver array. Additionally, the results of velocity measurement also for both P and S wave also agree with the result from semblance analysis.

By combine beamforming and semblance analysis, we are able to locate the source location, where figure 26 shows the result of our source location in yellow pin. Here, we are still able to extract the essential information from quarry blast via the workflow we purposed in main context. Additionally, we take the advantage of array sensors, and able to furthermore compute the directivity of the wave, hence located the blast.

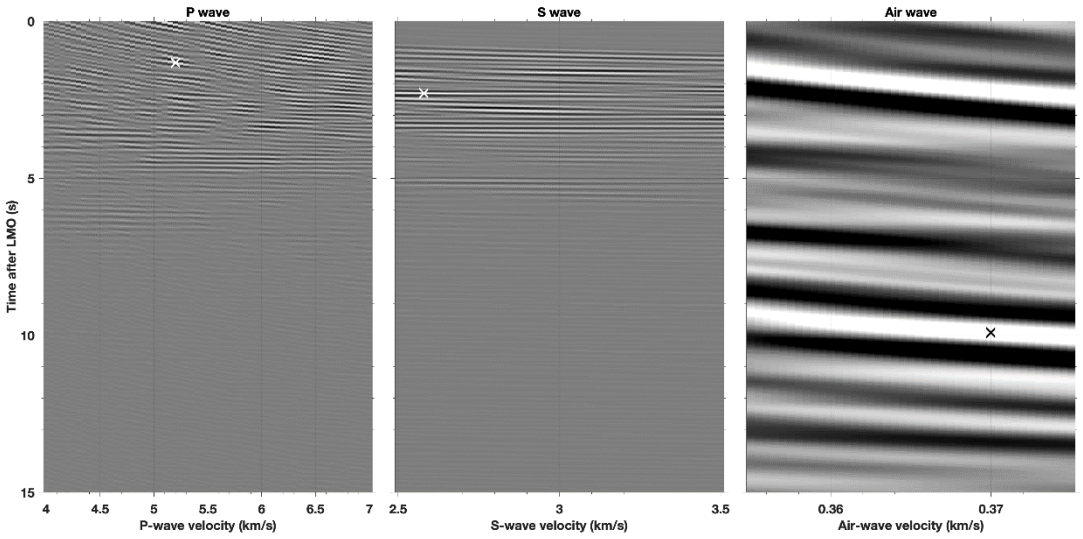

Figure 17: The semblance analysis for the first blast. The star (black and white) indicates maximum root mean square velocity. Since all the wave are generated from a same source location, hence, we can calculate the source distance with this velocity, and furthermore, depict the origin time prior to the onset time. Semblance analysis shows for P, S, and air wave are shown in (a), (b), and (c) respectively, and origin time and distance are documented in table 2.

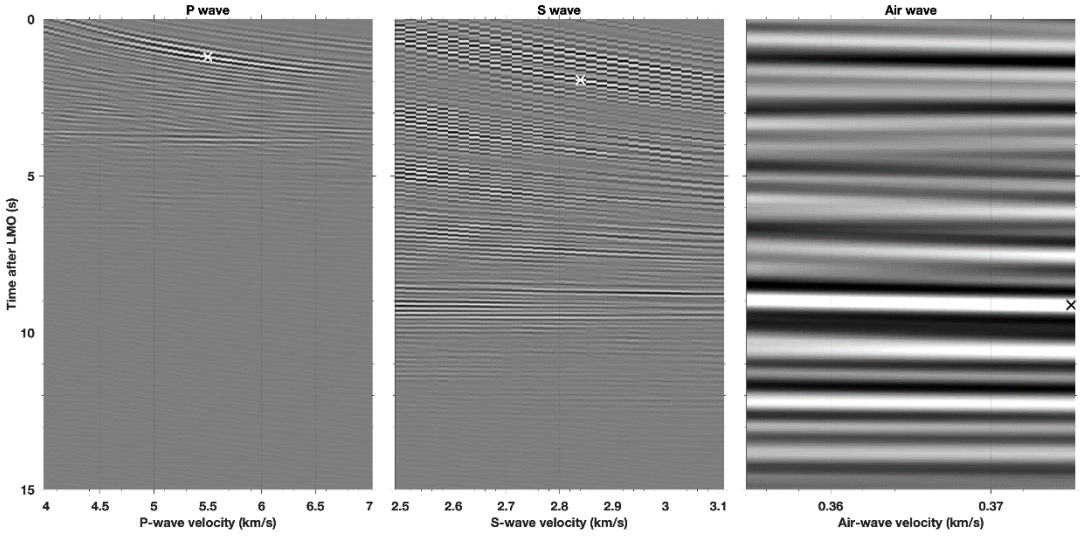

Figure 18: The semblance analysis for the second blast. The star (black and white) indicates maximum root mean square velocity. Since all the wave are generated from a same source location, hence, we can calculate the source distance with this velocity, and furthermore, depict the origin time prior to the onset time. Semblance analysis shows for P, S, and air wave are shown in (a), (b), and (c) respectively, and origin time and distance are documented in table 2.

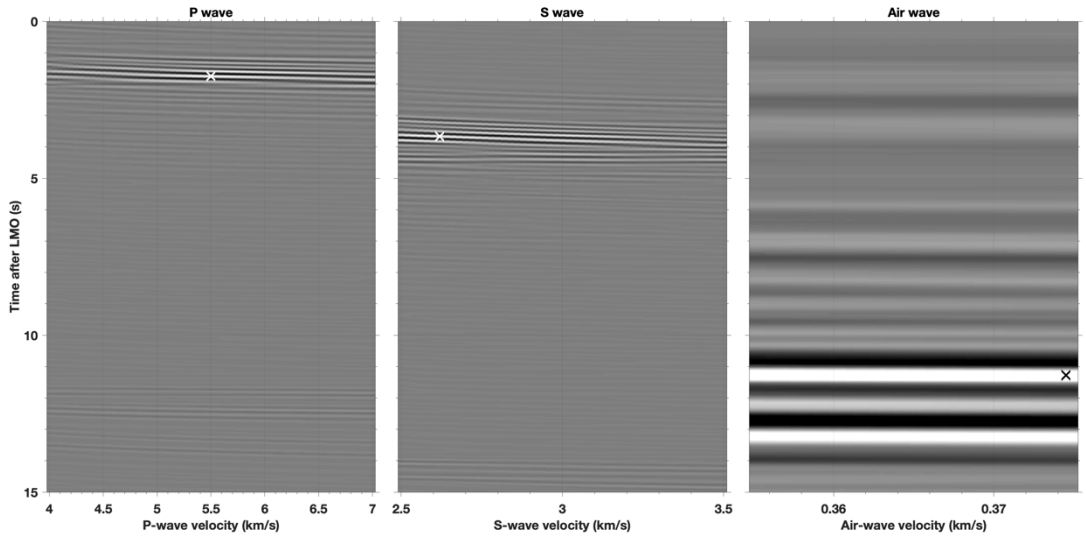

Figure 19: The semblance analysis for the third blast. The star (black and white) indicates maximum root mean square velocity. Since all the wave are generated from a same source location, hence, we can calculate the source distance with this velocity, and furthermore, depict the origin time prior to the onset time. Semblance analysis shows for P, S, and air wave are shown in (a), (b), and (c) respectively, and origin time and distance are documented in table 2.

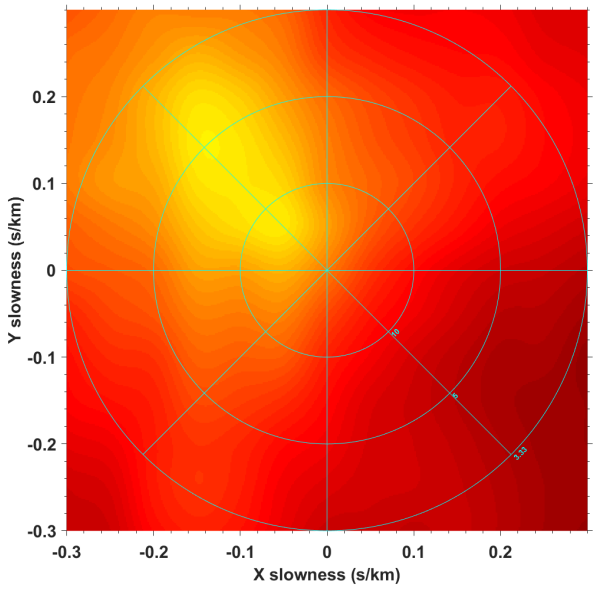

Figure 20: Beamforming analysis for P-wave recorded from blast in February 15th, 2018. The circle indicates the velocity, and the radius of the circle represents the velocity, from 10km/s to 5km/s and 3.33km/s from inside to outside circle respectively.The brighter the color, indicates the energy level is stronger. The brighter the color, indicates the energy level is stronger. And the orientation of the brightest color indicates that the azimuthal direction where the energy come from.

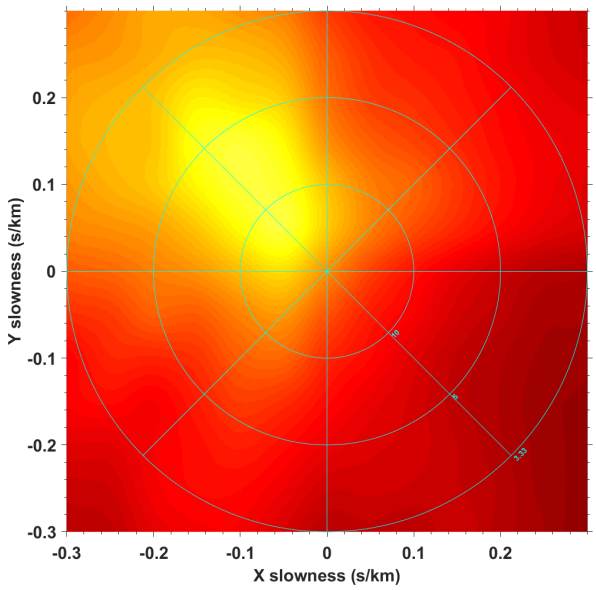

Figure 21: Beamforming analysis for P-wave recorded from blast in February 26th, 2018. The circle indicates the velocity, and the radius of the circle represents the velocity, from 10km/s to 5km/s and 3.33km/s from inside to outside circle respectively. The brighter the color, indicates the energy level is stronger. The brighter the color, indicates the energy level is stronger. And the orientation of the brightest color indicates that the azimuthal direction where the energy come from.

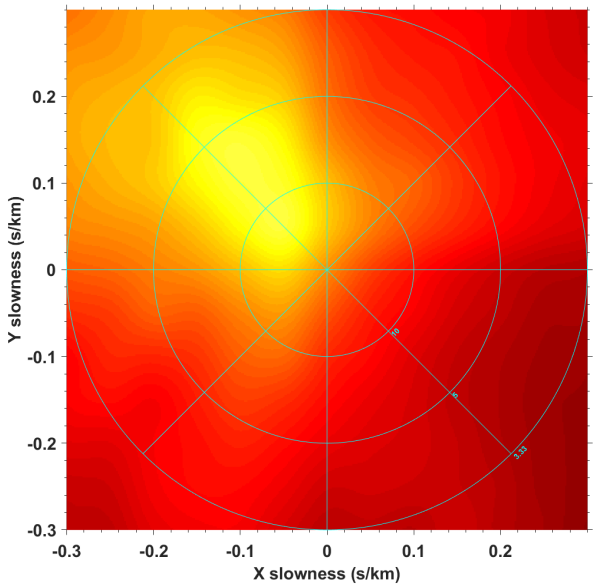

Figure 22: Beamforming analysis for P-wave recorded from blast in March 5th, 2018. The circle indicates the velocity, and the radius of the circle represents the velocity, from 10km/s to 5km/s and 3.33km/s from inside to outside circle respectively. The brighter the color, indicates the energy level is stronger. The brighter the color, indicates the energy level is stronger. And the orientation of the brightest color indicates that the azimuthal direction where the energy come from.

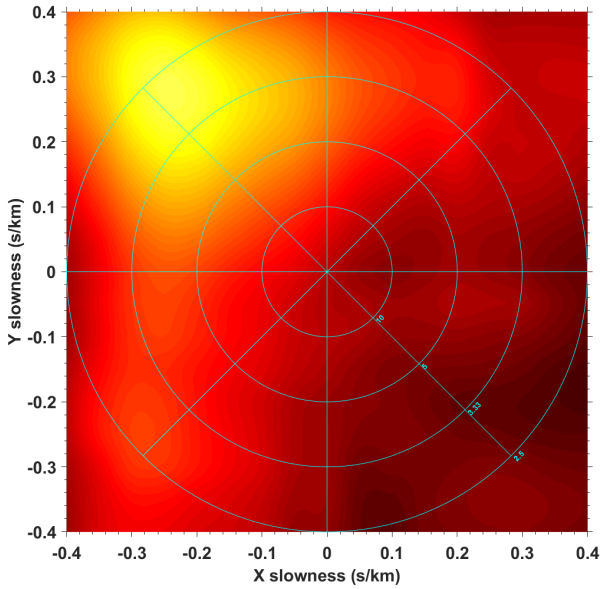

Figure 23: Beamforming analysis for S-wave recorded from blast in February 15th, 2018. The circle indicates the velocity, and the radius of the circle represents the velocity, from 10km/s to 5km/s and 3.33km/s and 2.5km/s from inside to outside circle respectively. The brighter the color, indicates the energy level is stronger. And the orientation of the brightest color indicates that the azimuthal direction where the energy come from.

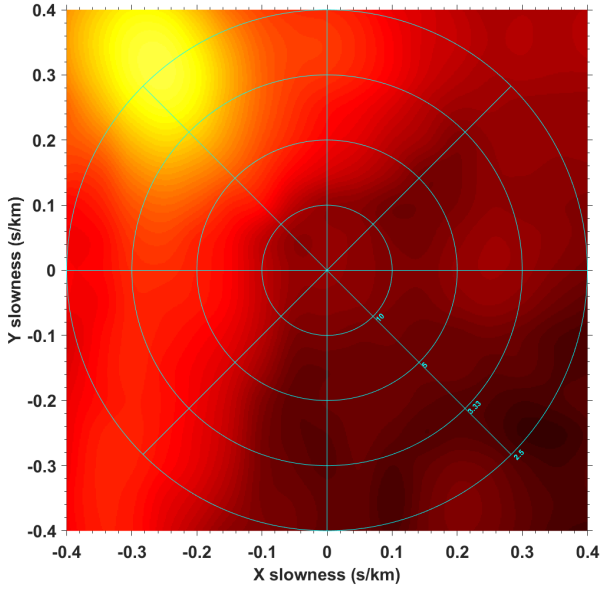

Figure 24: Beamforming analysis for S-wave recorded from blast in February 26th, 2018. The circle indicates the velocity, and the radius of the circle represents the velocity, from 10km/s to 5km/s and 3.33km/s and 2.5km/s from inside to outside circle respectively. The brighter the color, indicates the energy level is stronger. And the orientation of the brightest color indicates that the azimuthal direction where the energy come from.

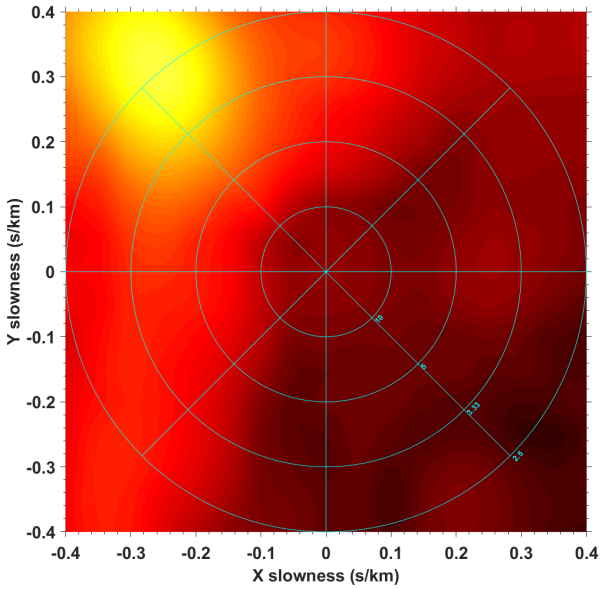

Figure 25: Beamforming analysis for S-wave recorded from blast in March 5th, 2018. The circle indicates the velocity, and the radius of the circle represents the velocity, from 10km/s to 5km/s and 3.33km/s and 2.5km/s from inside to outside circle respectively. The brighter the color, indicates the energy level is stronger. And the orientation of the brightest color indicates that the azimuthal direction where the energy come from.

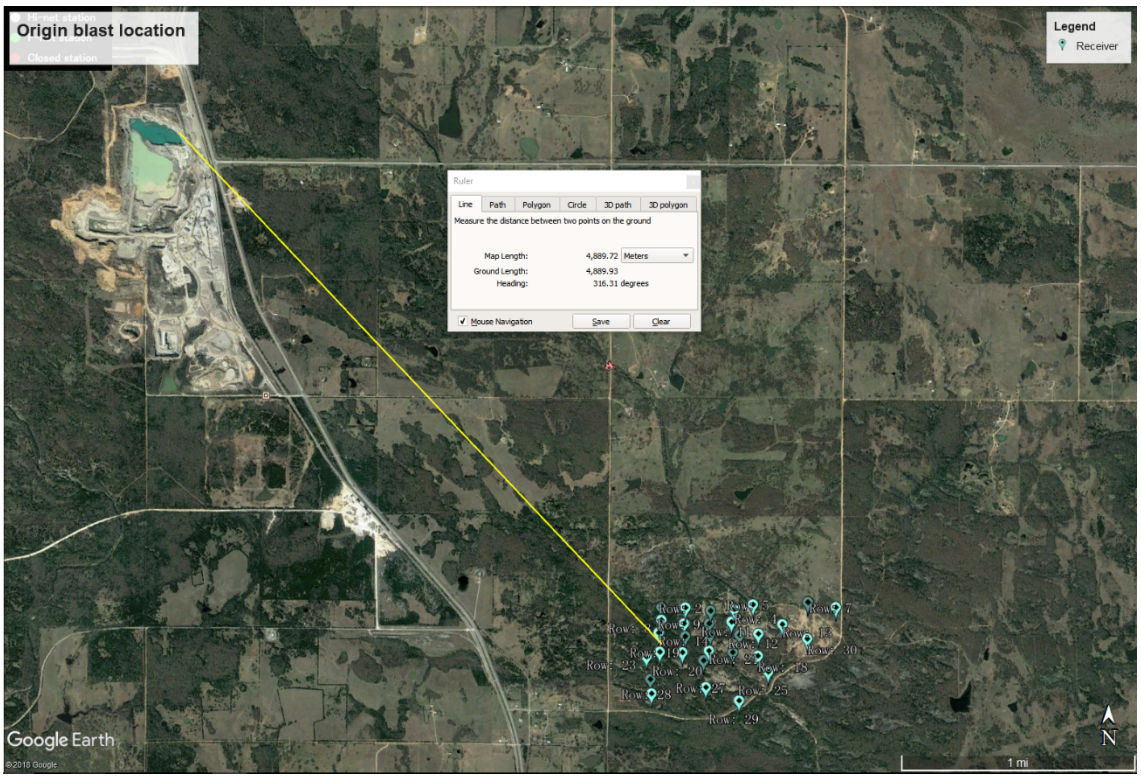

Figure 26: The result of blast location in a satellite view for third blast. We use the beamforming to examine the azimuthal orientation of the source and use the semblance analysis for the origin distance and time estimation.

	Origin time prior to onset time(sec)	*Origin distance from receiver 14(km)*	*P-wave velocity (km/s)*	*S-wave velocity (km/s)*	*Air wave velocity (km/s)*
Blast 1	0.394	4.93	5.2	2.58	0.37
Blast 2	0.322	4.87	5.5	2.84	0.375
Blast 3	0.88	4.89	5.5	2.62	0.3745

Table 2: Semblance results for three blasts from February to March 2018, total of 30 sensors are used.